1D inversion of multicomponent, multifrequency marine CSEM data: Methodology and synthetic studies for resolving thin resistive layers

Kerry Key[1]

ABSTRACT

Numerical methods for 1D forward modeling and inversion of marine controlled-source electromagnetic (CSEM) data are used to examine the inherent resolution of various acquisition configurations to thin resistive layers simulating offshore hydrocarbon reservoirs. Synthetic data studies indicate that jointly inverting frequencies of 0.1 and 1.0 Hz offers better resolution than inverting either frequency alone. Further increasing the bandwidth or density of frequencies does not produce a commensurate increase in resolution. An inline horizontal electric dipole is found to provide better resolution than either broadside or vertical electric dipoles. The horizontal electric and magnetic fields for any transmitter orientation have better resolution than vertical fields. Separate inversions of electric and magnetic fields perform equally well at recovering the reservoir, and there is no resolution improvement from jointly inverting both fields. Smooth inversion for a multiple resistive layer model detects the presence of all resistive layers, and shallow thin resistive layers do not impact the ability to image deeper resistive layers. The accuracy of the inverted models is improved substantially by including the boundary depths of resistive layers as a priori structure in the inversion. Including the seawater resistivity profile as fixed structure in the inversion is found to be essential for obtaining optimal resolution of subseafloor resistivity.

INTRODUCTION

The marine controlled-source electromagnetic (CSEM) method uses low-frequency electromagnetic energy generated by a deep-towed electric dipole to remotely quantify the seabed resistivity structure (e.g., Chave and Cox, 1982; Edwards, 2005). After field trials first demonstrated its usefulness for detecting offshore hydrocarbon reservoirs (Ellingsrud et al., 2002), marine CSEM began receiving a significant amount of commercial interest (e.g., Constable and Srnka, 2007). This interest has motivated studies of the physical behavior of CSEM in the presence of thin resistive hydrocarbon layers (e.g., Constable and Weiss, 2006; Um and Alumbaugh, 2007; Weidelt, 2007), encouraged efforts to extend this deepwater method to shallower water (e.g., Weiss, 2007; Andreis and MacGregor, 2008), and led to the creation of 2D and 3D modeling codes (Weiss and Constable, 2006; Li and Key, 2007; Gribenko and Zhdanov, 2007; Abubakar et al., 2008; Commer and Newman, 2008), among many other recent developments. Despite this level of activity, several fundamental aspects of marine CSEM remain unstudied in the published literature.

Consider some parameters required in the planning of a CSEM field survey. With the dipole transmitter systems now in use, complex waveforms can be designed to spread the transmitted energy across a band of discrete frequencies in a more even manner than the linear amplitude decrease of the traditional square wave (e.g., Mittet and Schaug-Pettersen, 2008). Ideally, the choice of the transmitter waveform should be guided by knowledge of the frequency bandwidth and density required to adequately image a specific target. However, there are direct trade-offs between frequency content and source dipole moment and hence signal-to-noise ratio in measured data. With these considerations in mind, it would be worthwhile to know how resolution depends on frequency content and whether there is a practical limit to improving resolution by increasing the frequency content. This knowledge then could serve to guide the selection of optimal transmitter waveforms.

There are many flavors of CSEM receivers available now. Some are capable of measuring all three components of the transmitted electric and magnetic fields, whereas others measure only some subset of the fields, such as only the horizontal components or only the electric fields. Yet, the relative value in acquiring each field type and component generally is not well known. Another factor is the orientation of the transmitter dipole. The most common acquisition method is to perform inline tows using a horizontal dipole, yet broadside and vertical transmitter orientations have been suggested as providing valuable information. Knowledge of how resolution varies as a

function of measured field components and transmitter orientation would be helpful for survey-planning tasks such as choosing a receiver system and laying out an acquisition geometry.

The purpose of this study is to present numerical algorithms for 1D CSEM forward modeling and inversion, and then to use inversions of synthetic data to examine the inherent resolution of 1D CSEM as a function of these survey parameters. Whereas previous studies have considered some aspects of 1D CSEM inversion for imaging offshore reservoirs (Constable and Weiss, 2006; Hoversten et al., 2006; Christensen and Dodds, 2007), there is a need for a systematic investigation of how the resolution depends on the frequency content, transmitter orientation, and recorded field components. This information could be useful to geophysicists planning offshore CSEM field campaigns.

METHODOLOGY

This section reviews the forward and inverse modeling methodology used for the synthetic inversions. Methods for computing the forward responses of dipoles embedded in multilayered 1D media are well studied (e.g., Stoyer, 1977; Chave and Cox, 1982; Ward and Hohmann, 1988; and many others). The approach used here follows the magnetic vector potential formulation described in Wait (1982), but generalizes this formulation to allow for multiple layers above the transmitter (in addition to multiple layers below), and uses exponential forms for the recursions rather than hyperbolic functions. Only isotropic conductivity is considered here, but readers interested in 1D methods for transversely isotropic and generally anisotropic media are referred to Xiong (1989) and Løseth and Ursin (2007), respectively. An overview of the 1D formulation is given below, and more specific details are provided in Appendices A–C.

Modeling an electric dipole in 1D

Consider the 1D model shown in Figure 1, which consists of N layers of isotropic conductivity σ_i where $i = 1, \ldots, N$, and which uses a right-handed coordinate system with the z axis pointing down. Assuming a time-harmonic source with $e^{-i\omega t}$ time dependence, negligible magnetic permeability μ variations, and angular frequencies
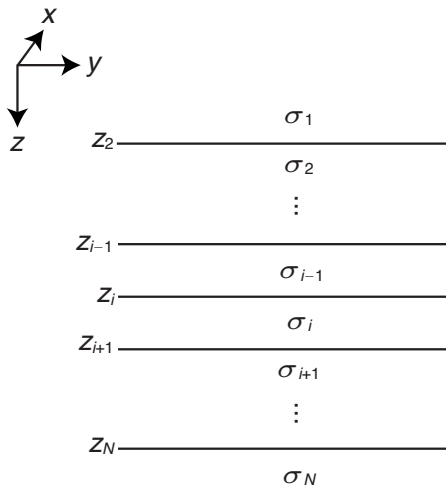

Figure 1. The N-layered 1D model. Each layer i has conductivity σ_i and layer top depth z_i. The top and bottom layers extend to infinity along z. The transmitters and receivers can be located in any layer.

ω that are low enough so that displacement currents can be neglected, Maxwell's equations are

$$\nabla \times \mathbf{E} = i\omega \mathbf{B}, \tag{1}$$

and

$$\nabla \times \mathbf{B} = \mu\sigma \mathbf{E} + \mu \mathbf{J}_s. \tag{2}$$

Expression $\mathbf{J}_s = \mathbf{I}\delta(\mathbf{r} - \mathbf{r}_0)$ is the imposed electric dipole source at position $\mathbf{r}_0$ with vector moment $\mathbf{I}$, and here is restricted to be an infinitesimally small dipole with unit moment. Using the magnetic vector potential $\mathbf{A}$, the magnetic field $\mathbf{B}$ is specified as

$$\mathbf{B} = \nabla \times \mathbf{A}. \tag{3}$$

From equations 1–3, the electric field $\mathbf{E}$ can be found to be

$$\mathbf{E} = i\omega \mathbf{A} + \frac{1}{\mu\sigma} \nabla (\nabla \cdot \mathbf{A}), \tag{4}$$

where the Lorenz gauge has been specified. The vector potential can be obtained from the solution of the Hankel transform equation

$$\mathbf{A}(\mathbf{r}) = \frac{1}{2\pi} \int_0^\infty \hat{\mathbf{A}}(\lambda, z) J_0(\lambda r) \lambda d\lambda, \tag{5}$$

where J_0 is a zeroth-order Bessel function of the first kind and r is the horizontal range.

Recursive formulas for computing the transform kernel $\hat{\mathbf{A}}$ for horizontal and vertical electric dipoles located at arbitrary depth in the layered model are given in Appendices A and B. In practice, the electric and magnetic fields are computed directly by inserting equation 5 into equations 3 and 4. The fields produced by arbitrarily oriented dipoles are computed using the vector superposition of the fields produced by horizontal and vertical transmitters.

Occam's inversion

The inverse problem is to find a conductivity model compatible with a given data set, and solutions to this problem are well described throughout the electromagnetic (EM) geophysics literature (e.g., Parker, 1994; Zhdanov, 2002, and references therein). Because a given data set is finite and imprecise, an infinite number of solutions to the inverse problem exist. A standard method for handling this nonuniqueness is to restrict the set of acceptable solutions to those that meet some a priori constraints on model structure, otherwise known as the regularized inverse problem. The model studies here use Occam's inversion method (Constable et al., 1987), which solves the regularized problem by searching for the smoothest model that fits the data. The utility of this method is that it generally produces smooth peaks in the model that correspond to features that are well constrained by the data, whereas features not constrained by the data will be smoothed over or entirely absent in the model. A brief review of the Occam's inversion approach is given below.

The regularized inverse problem seeks to minimize the functional

$$U = \|\boldsymbol{\partial}\mathbf{m}\|^2 + \|\mathbf{P}(\mathbf{m} - \mathbf{m}_*)\|^2 + \mu^{-1}$$

$$\times[\|\mathbf{W}(\mathbf{d} - F(\mathbf{m}))\|^2 - \chi_*^2]. \qquad (6)$$

The first term is a norm of the model roughness and is computed by applying a differencing operator $\boldsymbol{\partial}$ to the elements of the model vector $\mathbf{m}$. For the 1D models considered here, $\mathbf{m}$ is a vector of $\log_{10} \sigma$ for each layer, and $\boldsymbol{\partial}$ is chosen to be a matrix of first-differencing operators so that $\boldsymbol{\partial}\mathbf{m}$ approximates the vertical derivative of $\log_{10} \sigma$. The parameterization with respect to $\log_{10} \sigma$ ensures that conductivity remains positive during the inversion. If jumps in conductivity are desired at certain depths, the corresponding elements of $\boldsymbol{\partial}$ can be set to zero.

The second term is a measure of the difference of $\mathbf{m}$ from an a priori preference model $\mathbf{m}_*$. The diagonal matrix $\mathbf{P}$ contains scaling parameters that determine the relative weighting between the preference and model roughness. Preference model values, if used at all, typically are desired for only a few model layers, and the corresponding diagonal elements of $\mathbf{P}$ will be nonzero.

Finally, the third term is a measure of the misfit of the model's forward response $F(\mathbf{m})$ (i.e., the electric and magnetic fields for model $\mathbf{m}$) to the data $\mathbf{d}$. There is no restriction on the data vector $\mathbf{d}$. For example, it can contain data from multiple transmitters, receivers, and frequencies. Expression $\mathbf{W}$ is a data covariance weighting function and is selected here to be a diagonal matrix with elements corresponding to inverse data standard errors. In other words, $\mathbf{W}$ weights the relative contribution of each datum to the misfit based on its uncertainty. Thus, data with large errors are scaled to limit their influence, whereas data with small errors will have a bigger impact on the misfit budget.

Expression χ_*^2 is the target misfit, and its inclusion illustrates that minimizing U does not necessarily find the best-fitting model, but rather a smooth model that is within the specified target misfit. The Lagrange multiplier μ serves to balance the trade-off between the data fit and the model roughness and model preference.

The standard method for minimizing U in equation 6 is to take the derivative with respect to $\mathbf{m}$ and set it equal to zero. Because the derivative of $F(\mathbf{m})$ is nonlinear in electromagnetics, the resulting equation is solved iteratively by creating a sequence of models, each of which gradually provides a better fit to the data. After linearizing about an initial model $\mathbf{m}_k$, the equation for the next model in the sequence $\mathbf{m}_{k+1}$ is

$$\mathbf{m}_{k+1} = [\mu(\boldsymbol{\partial}^T\boldsymbol{\partial} + \mathbf{PP}) + (\mathbf{WJ}_k)^T\mathbf{WJ}_k]^{-1}$$

$$\times[(\mathbf{WJ}_k)^T\mathbf{W}\hat{\mathbf{d}} + \mu\mathbf{Pm}_*], \qquad (7)$$

where

$$\hat{\mathbf{d}} = \mathbf{d} - F(\mathbf{m}_k) + \mathbf{J}_k\mathbf{m}_k. \qquad (8)$$

Expression $\mathbf{J}_k$ is the linearized model response gradient, or Jacobian matrix

$$\mathbf{J}_k = \nabla_{\mathbf{m}}F(\mathbf{m}_k), \qquad (9)$$

with elements

$$J_{ij} = \frac{\partial F_i(\mathbf{m}_k)}{\partial \log_{10} \sigma_j}, \qquad (10)$$

where $i = 1, \ldots, n$, $j = 1, \ldots, m$, and n is the number of data and m the number of model layers. In other words, $\mathbf{J}$ is a sensitivity matrix containing the derivative of each field component with respect to $\log_{10} \sigma$ in each layer. A method for efficiently computing $\mathbf{J}$ for 1D CSEM is given in Appendix C.

To solve equation 7, one must choose a value of the Lagrange multiplier μ. The approach used by Occam's method (Constable et al., 1987) is to perform a golden section search through μ to find the model $\mathbf{m}_{k+1}(\mu)$ with the best fit to the data, which initially will probably be greater than the target misfit. The model update iterations are continued in this manner until the target misfit χ_*^2 has been reached, at which point Brent's method is used to find the intercepts. There can be more than one intercept of χ_*^2 along μ, and the model with the largest μ is chosen because it will tend to be the smoothest model. In practice, the target misfit χ_*^2 usually is chosen so that the root mean square (rms) misfit x_{rms} is equal to unity,

$$x_{rms} = \sqrt{\frac{\chi^2}{n}} = \sqrt{\frac{1}{n}\sum_{i=1}^{n}\left[\frac{d_i - F_i(\mathbf{m}_{k+1}(\mu))}{s_i}\right]^2},$$

$$(11)$$

where n is the number of data and s_i is the standard error of the ith datum.

Implementation and validation

The forward modeling and sensitivity methods have been implemented into a Fortran 90 code named Dipole1D. This code is generalized so that the dipole and observation points can reside anywhere in the stack of layers, the dipole can have arbitrary orientation and dip, there are no fixed assumptions of seawater layers, and all components of $\mathbf{E}$ and $\mathbf{B}$ are computed. The Hankel transforms are evaluated using the digital filter method (e.g., Ghosh, 1971; Anderson, 1982; Kong, 2007), with 201-point J_0 and J_1 filters designed by using an optimization technique similar to the method given in Guptasarma and Singh (1997).

The digital Hankel transforms require the computation of the potential coefficients a_i, b_i, c_i, d_i (given in Appendix A and B) over a discrete range of logarithmically varying λ, where the discrete λ depend on the source-receiver offset. Because the coefficients vary smoothly as a function of λ, the Hankel transforms are computed rapidly for many receivers by precomputing the coefficients over a range of λ, and then using cubic spline interpolation during the transform computations for specific source-receiver offsets.

Forward responses computed with Dipole1D have been validated by comparison with results from an earlier code based on Chave and Cox (1982) and Flosadottir and Constable (1996), and with results from a 2D finite-element code presented in Li and Key (2007). The sensitivity computations were verified by comparison with brute-force forward differences for small perturbations in layer conductivities. To validate the section of the code that allows for multiple layers above the transmitter, which is not possible with the Flosadottir and Constable (1996) code, the 1D layering was flipped vertically about a line of receivers along the seafloor, and the results were validated by noting that the response symmetry was maintained.

The 1D CSEM inversion has been implemented using a Fortran 90 version of Occam, which is coded so that the forward, sensitivity, and roughness computations are decoupled from the main inversion routines. Thus interfacing Occam with forward routines for any specific geophysical method (EM, gravity, seismics, and so forth) is

quite simple. For the 1D CSEM implementation, Occam makes external calls to the forward and sensitivity computation routines contained in Dipole1D. The inversion models considered here used 75 unknown model parameters (i.e., layer resistivities); the number of data varied from 500 to 6000, depending on the number of components and frequencies under consideration. The inversions typically converged to rms 1.0 misfit within 10–20 Occam iterations, requiring about 1–2 minutes of CPU time on a 2.33 GHz laptop.

SYNTHETIC INVERSION TESTS

This section presents synthetic inversion studies that examine how the resolving capabilities of CSEM depend on the transmitter's orientation and frequencies, and on the inverted electric and magnetic field components. For these studies, synthetic noisy data are inverted using Occam's method to find the smoothest model required to produce the features in the data. Thus, the smooth inversion is used to provide a measure of the inherent resolution of each data set under consideration.

The base model for these studies is the canonical 1D reservoir that was considered previously in Constable and Weiss (2006), and is shown in Figure 2. This model consists of a 100-ohm-m resistive reservoir of 100-m thickness located 1 km beneath the seafloor, with surrounding 1-ohm-m sediments. The conductive ocean is 1 km deep, and the transmitter is located 25 m above the seafloor. A single receiver is positioned on the seafloor at $y = 0$, and CSEM responses are computed for transmitters located at 50-m intervals from 0 through 20 km in y. In practical terms, this corresponds to a data set obtained from selecting 60-s windows of transmission at a 1.5-knot tow speed.

Synthetic data sets were created by adding normally distributed random noise to the model responses. Because this study's objective is to examine the relative merits of different data components, and not the effects of noise level on inversion, an optimistic, low noise level of 1% was used. The 1% noise was computed relative to the response amplitudes and generated separately for real and imaginary components of the complex data. A minimum absolute noise level (i.e., the transmitter-receiver-system noise floor) was set to

10^{-15} V/Am^2 for electric fields **E** and 10^{-18} T/Am for magnetic fields **B**, and data below this minimum level were eliminated from the synthetic data set. Whereas short-offset amplitudes are well above this absolute noise floor, the 1% relative noise is a simple way to mimic the increased relative uncertainty in the navigated source-receiver vector at short offsets. To circumvent phase-wrapping difficulties, the complex data were inverted as real and imaginary components.

An example of the synthetic noisy data, an inversion model's responses, and normalized residuals of the model fit are shown in Figure 3. The normalized residuals (the quantity between the brackets in equation 11) are generally uncorrelated with source-receiver offset (range) and are normally distributed about a zero mean, indicating that the inversion is not biased to either the short- or long-offset data, and that the noise model can be well fit by the inversion. For the inversions considered here, preference models have not been used (i.e., **P** in equation 6 is set to 0).

The first test examines how the inverted models vary over several realizations of random noise. Ideally, the inverted models won't vary much, so they will reflect the inherent resolution of the particular combinations of frequencies and field components, rather than variations in the specific noise realizations. Figure 4 shows the range of resistivities obtained for inverting E_y from inline (y) transmissions with 10 different realizations of 1% noise for 0.1-Hz data and 1.0-Hz data, where each data set was fit to rms 1.0. The resistivity range in the models is quite small. At depths below the reservoir, the 1-Hz model has a higher resistivity range, reflecting the fact that its data have less sensitivity to structure at these depths because it only contains data to a 7-km range, where it intersects the system noise floor. However, the main features of the inversion models do not vary much for either frequency, suggesting that they result from the resolution of the particular data coupled with the regularization smoothness constraint, rather than from any particular noise realization.

Effect of inverting multiple frequencies

This test examines the improvements in resolution from including multiple frequencies in the data. Although it seems obvious that including more frequencies should lead to improved resolution, it is worthwhile to study the extent of this improvement with respect to the frequency bandwidth and density. Before inverting any data, some insight can be gained by plotting the responses as a function of frequency, and this can serve also to guide the selection of discrete transmission frequencies. Figure 5 shows the inline electric-field (E_y) frequency responses at 1-km and 4-km source-receiver offset for a 1-ohm-m half-space, the canonical model, and the multiple resistive layer model (shown later). The responses for all three models are nearly the same at low frequencies and are asymptotic to a DC value at the lowest frequencies (about 0.1–0.01 Hz).

At high frequencies, at which inductive attenuation becomes important, the responses decay rapidly and exhibit substantial differences among the models. At 1-km offset, the multilayer response has larger amplitudes because it contains a 25-m-thick, 5-ohm-m resistive layer at the seafloor, whereas the half-space and canonical model responses are indistinguishable. At 4-km offset, the canonical and multilayer responses have considerably larger amplitudes than the half-space response, and the multilayer response is slightly larger
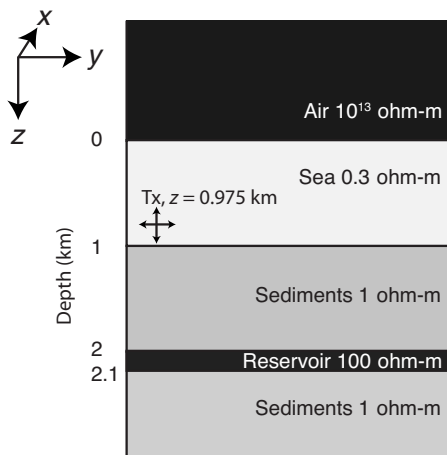

Figure 2. The canonical 1D reservoir model used for the synthetic inversion studies. The 100-m-thick reservoir is 100 ohm-m and resides 1000 m below the seafloor. The transmitter (Tx) is located 25 m above the seafloor at 975-m depth and is towed along the y axis from 0 through 20-km range.
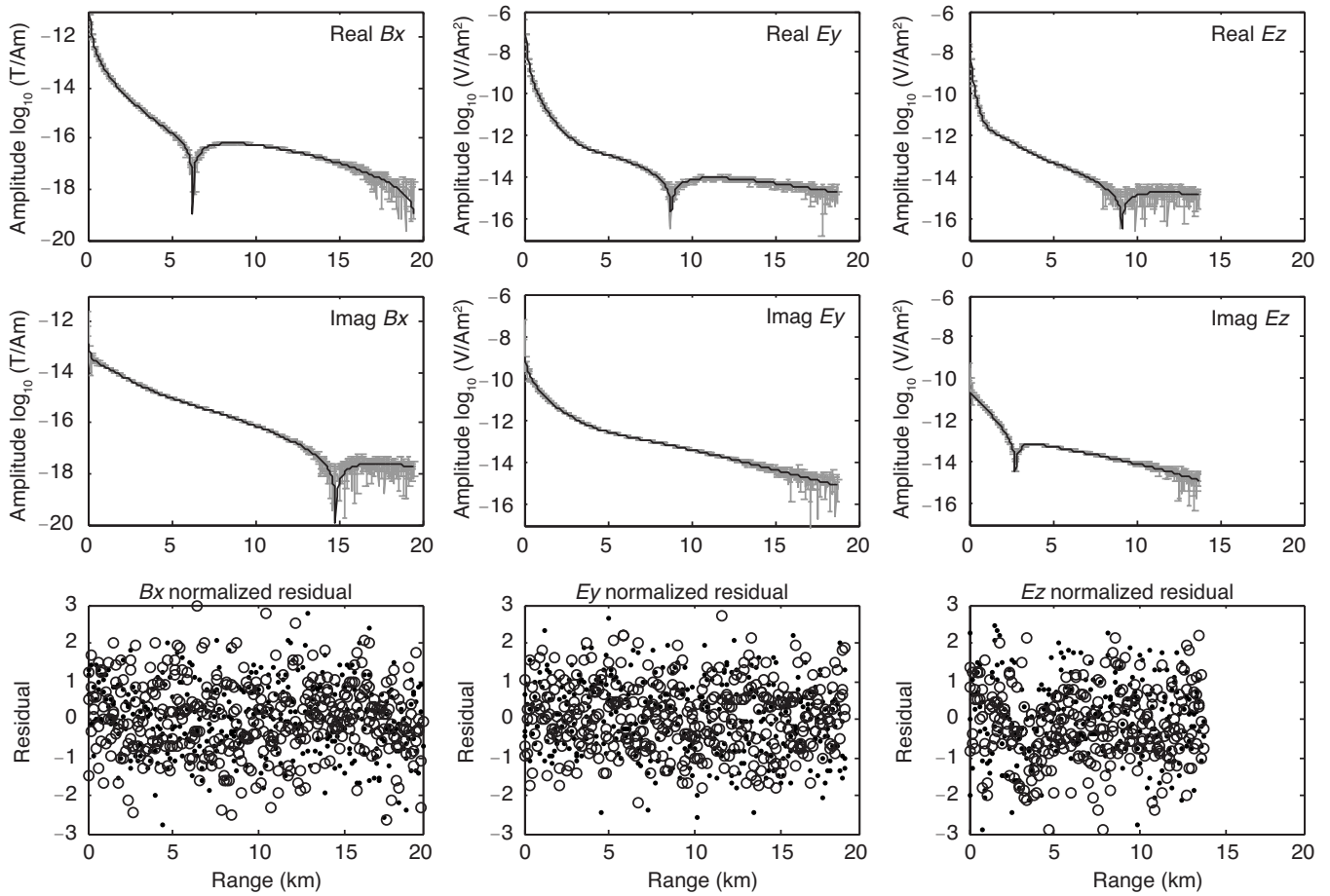
Figure 3. Example of synthetic 0.1-Hz data and inversion model fits (black line) for the model study shown in Figure 8. Vertical gray bars show the 1% standard error, subject to an error floor of 10^{-15} V/Am² for the electric field and 10^{-18} T/Am for the magnetic field. The bottom row shows the normalized residuals of the model fit for real (dots) and imaginary (circles) components. The rms misfit is 1.0.
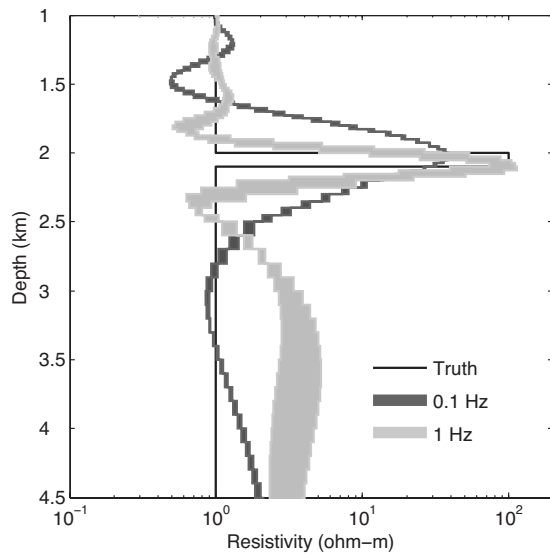

Figure 4. Variations in the synthetic inversions for an ensemble of noise realizations. The shaded regions show the minimum and maximum resistivity obtained from inverting E_y with 10 different realizations of 1% normally distributed random noise for 0.1-Hz data (dark gray) and 1.0-Hz data (light gray). The black line shows the true model. All models fit the data to rms 1.0.
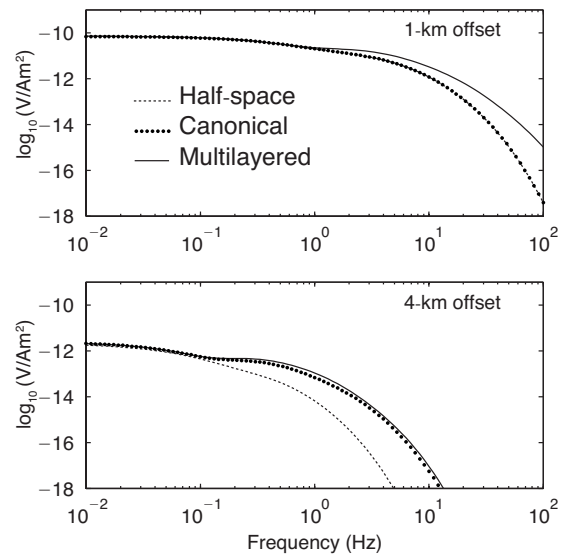

Figure 5. Frequency responses for the inline electric field amplitude at 1-km (top) and 4-km (bottom) source-receiver offsets. Responses are shown for a seafloor half-space, the canonical 1D model, and the multilayered model shown in Figure 8, as indicated in the legend.

than the canonical model because of the additional shallow resistive structure. These responses suggest that a DC transmitter would have difficulty identifying shallow structure above a reservoir, but that short-offset, high-frequency data would aid greatly in distinguishing shallow from deep structure.

Overall, the responses vary smoothly with frequency, and this suggests that there would be a limit to improvement in resolution gained by increasing the frequency density in inverted data. For instance, these curves could be described fairly well by only a few discrete frequencies per $\log_{10}$ decade. Based on the behavior of these curves, it seems that data in the range of 0.1–10 Hz would be most useful for characterizing these structures.

Three variable-frequency synthetic data sets were created using the inline electric-field (E_y) responses from a horizontal transmitter. Figure 6 shows the results for inverting a single frequency (1 Hz), two frequencies (0.1 and 1 Hz), and five frequencies (0.1, 0.3, 1, 3, and 10 Hz). All three combinations recover the reservoir layer equally well, but the sediment resistivity beneath the reservoir is overestimated by the 1-Hz data because it has low sensitivity to

Figure 6. The effect of frequency content on 1D resolution. Synthetic inversion models are shown for inversion of E_y data with a variable number of discrete transmission frequencies, as indicated in the legend. All models fit the data to rms 1.0.

Figure 7. The resolution of the **E** and **B** field components for the three fundamental transmitter orientations (broadside x, inline y, and vertical z). Synthetic inversion models are shown for inversion of each component separately and all three together, as indicated in the legends. The transmission frequencies were 0.1 and 1.0 Hz, and all models fit the data to rms 1.0.

these depths. There is little difference between the two- and five-frequency inversions, suggesting that a limit has been reached for improving resolution by increasing the frequency density and bandwidth.

This study has practical importance because it can serve as a guide to selecting a transmission waveform for field surveys. The results here suggest that waveforms producing many finely spaced transmission frequencies are unnecessary because the CSEM responses vary smoothly in frequency. The inversion models show a significant improvement when two widely spaced frequencies are used, but further extension of the bandwidth and density of frequencies yields no appreciable increase in resolution. Thus, it seems that an optimal waveform would concentrate most of the transmitted energy in only a few widely spaced frequencies.

Effect of transmitter direction and field components

It has long been known that horizontal transmitters create a richer data set than vertical transmitters (e.g., Chave and Cox, 1982), and today the most commonly collected and interpreted data are the inline electric fields obtained from a horizontal transmitter. However, many marine EM receiver systems now in use are capable of recording all three components of both electric and magnetic fields, and many surveys have used grids of receivers and transmitter towlines. It is worthwhile to examine if resolution can be improved by inverting multiple field components, and how resolution varies with the transmitter orientation.

There are three fundamental dipole orientations: x, y, and z. For 1D models with transmitters and receivers along the y axis, an x-(broadside) oriented transmitter will generate E_x, B_y, and B_z field components. Conversely, y-(inline) and z-(vertically) oriented transmitters will generate B_x, E_y, and E_z field components. Figure 7 shows results for inverting each field component for each transmitter orientation separately, and for jointly inverting all three components for each transmitter orientation. For all transmitter orientations, the z field-component inversions perform the worst. In particular, the B_z component for a broadside (x) transmitter is the only inversion that does not recover a resistive layer in the vicinity of the reservoir. This is expected, given that Faraday's law shows that B_z is associated only with horizontal current flow.

In general, the horizontal electric and magnetic field components detect the reservoir and have nearly identical models. When all three components are inverted together, there is no appreciable improvement over the inversions of a single horizontal component. A fundamental difference between the inverted models is the systematic variation with transmitter orientation. Clearly, the inline (y) transmitter inversions recovered the resistivity, thickness, and depth of the reservoir much better than either the broadside or vertical transmitter inversions. In addition, the broadside and vertical transmitter inversions performed less well at recovering the resistivity of deeper sediments. It is worth pointing out that the similarity of the E_z inversion for a y transmitter to the E_y inversion for a z transmitter is predicted from electromagnetic reciprocity.

Although not shown here, an inversion of both broadside and inline data produces a model with nearly identical structure to the inline-only inversion. This is in disagreement with a previous
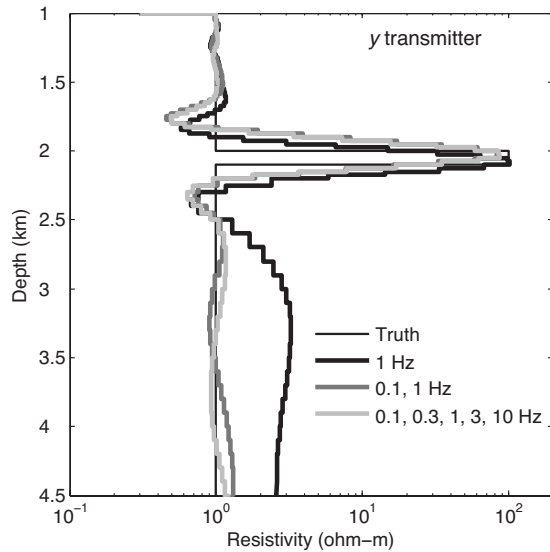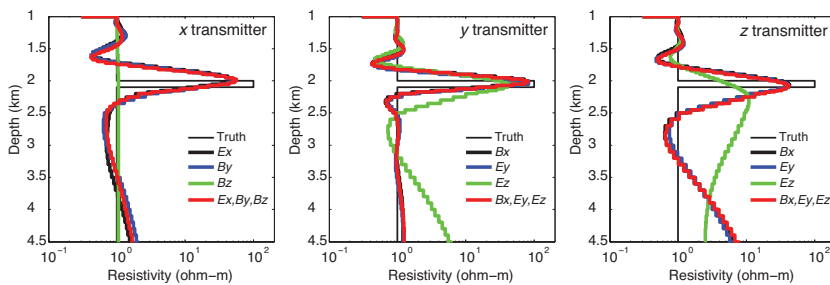
study, which showed that including broadside data can aid greatly in resolving thin from thick resistors (Constable and Weiss, 2006). However, that study considered only amplitude data, which for inline transmissions is sensitive predominantly to galvanic effects associated with the reservoir's resistivity-thickness product. The authors found that by also including broadside amplitude data also, which is sensitive to induction in the conductive sediments above and below the reservoir, the inversion can discriminate between the reservoir thickness and resistivity. The studies here have considered both inline amplitude and phase data, suggesting that phase data, which is only modified through inductive effects in the conductive regions of the model, also allows the inversion to distinguish reservoir thickness from resistivity.

Because the vertical field inversions performed poorly, and there is no improvement when jointly inverting the vertical and horizontal fields, the utility of measuring the vertical electric and magnetic field components remains unclear. Significant reservoir lateral-edge effects have been observed in the horizontal and vertical electric fields (Constable and Weiss, 2006), and it probably will require 2D or 3D inversion studies to address whether including the vertical fields could offer improved resolution. Another implication concerns the utility of measuring both electric and magnetic fields. Given that the magnetic field inversions performed as well as the electric field inversions and there is no improvement in combining these data, perhaps only one measurement is needed. There might be practical applications such as remotely operated vehicle (ROV) deployments, in which the smaller footprint of a magnetometer-only instrument is desired, or there might be instances in which sea-bottom cables contain only inline electric field dipoles.

Although ultimately it would depend on many factors, including the specific sensor noise levels, these model resolution studies suggest the viability of acquiring either electric or magnetic fields alone. However, for the standard CSEM field operations now in practice, the cost of recording both fields is relatively low compared with total operational costs, and the redundancy in sensitivity obtained by recording both fields can be used as mitigation against unforeseen failures of individual component recordings. Furthermore, there could be benefits to 2D and 3D modeling when electric and magnetic fields are inverted, but this remains to be studied in the published literature.

Inversion with multiple resistive layers

Although the canonical model is useful for establishing insights, more complicated structures must be considered. Figure 8 shows an extension of the canonical model that includes multiple resistive layers. At the seabed lies a 25-m-thick, 5-ohm-m resistive layer representative of shallow gas or methane hydrate. Another layer resides 500 m below the seabed and is 50 m thick with a 10-ohm-m resistivity. The model is terminated by a 10-ohm-m basement beginning at 4-km depth. The E_y frequency response of this model for an inline transmitter was shown in Figure 5. Despite the introduction of additional resistive structure, the frequency responses are only moderately different from the canonical model.

Synthetic inversions of two frequencies (0.1 and 1 Hz) and five frequencies (0.1, 0.3, 1, 3, and 10 Hz) are shown in Figure 8. Both inverted data sets recover resistive features in the general location of the true layers. The resistivity and depth extent of the shallow hydrate layer are the best-recovered features among the several resistive layers. Despite the overlying resistive layers, the reservoir is re-

covered with nearly the same accuracy as for the canonical model studies, suggesting that shallow resistive structure does not impede the detection of deeper structures.

The inversions are nearly identical for the two data sets, with the exception that the five-frequency data recovered the subreservoir sediment resistivity slightly better than the two-frequency data. Both data sets recovered an increase in resistivity at basement depths, but neither did a good job of identifying the sharp boundary of this increase. With the exception of the shallow hydrate layer, overall the resistive features were recovered as highly smoothed bumps in resistivity.

Inversion with a priori constraints on boundary depths

Although smooth inversion could be useful for identifying whether potential targets are resistive, it does not produce a model accurate enough to be useful for quantitative interpretation. For example, reservoir properties such as saturation and porosity can be estimated by jointly interpreting seismic and CSEM data (e.g., Hoversten et al., 2006), but using a smooth model for this would lead to inaccurate estimates of reserves. More quantitative results can be obtained if the depths of structural boundaries can be constrained a priori. In many cases, CSEM data are collected after seismic acquisition, and thus structural boundaries identified in the seismic interpretation can be used to improve CSEM modeling. For example, MacGregor and Sinha (2000) found that synthetic inversion better recovers the bottom depth of a resistive basalt layer when the roughness penalty is relaxed along the top of the basalt.

Figure 9a shows an inversion using the same layering as in the previous studies, but with the roughness penalty removed at the resistive layer boundary depths. Remarkably, the inversion recovers the uniform resistivity within each structural layer, and the resistivities are close to their true values. Figure 9b shows the relative error in the resistivity of inverted model layers compared with the true mod-
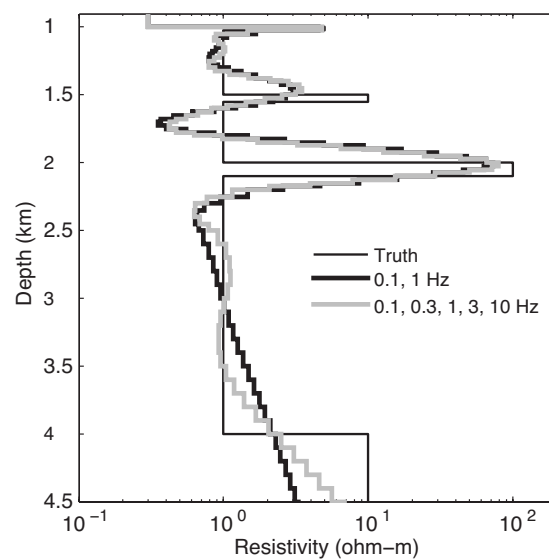

Figure 8. Synthetic inversion tests for a model with multiple resistive layers: B_x, E_y, and E_z data for inline (y) transmissions were inverted for various combinations of frequencies, as shown in the legend. Both models fit the data to rms 1.0.

el. The resistive layers and sediments are recovered to about 1% error, whereas the deep basement layer is less well resolved with about 30% error. Obviously more complicated scenarios should be considered, as well as the effect of using inaccurate boundary depths. However, this example serves to illustrate the level of accuracy possible with high-quality CSEM data and well-determined a priori structural boundary constraints.

Effect of fine-scale resistivity variations

The offshore environment undoubtedly contains more structural variability than considered in the previous model studies, particularly with respect to porosity variations resulting from lithology, grain size, and compaction. This section simulates the effects of fine-scale variability by creating a model consisting of 1000 layers of random, uniformly distributed thicknesses between 0 and 10 m, and assigning a porosity to each layer using a compaction model with random
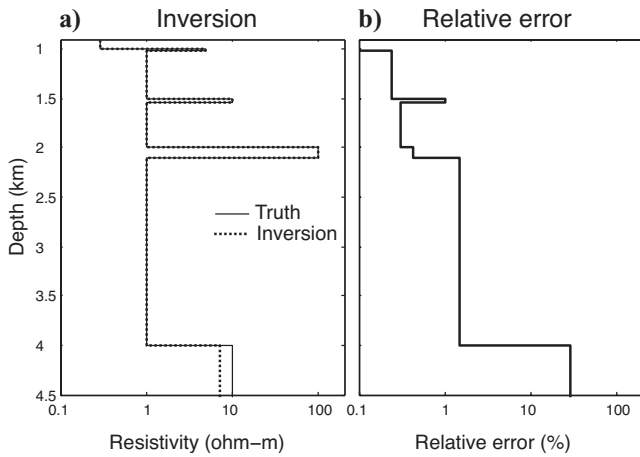
Figure 9. Synthetic inversion test with the roughness penalty removed across the top and bottom of the resistive layers. The (a) inversion model used the same five-frequency data set used for Figure 8 and consisted of B_x, E_y, and E_z data for inline (y) transmissions. The (b) relative error shows the relative difference in linear resistivity between the true model and inversion model.
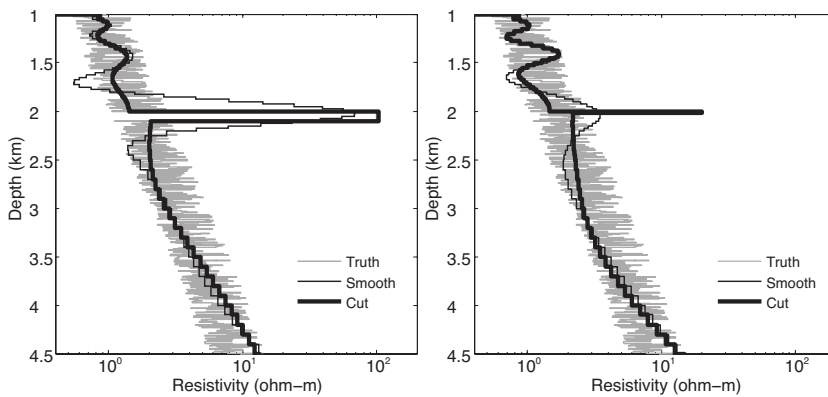
Figure 10. Synthetic inversion tests for a model with fine-scale porosity variations (thin gray line) for the (left) canonical 1D reservoir and (right) a smaller reservoir that is 20 m thick and 10 ohm-m. Inline B_x, E_y, and E_z data at 0.1 and 1.0 Hz were inverted using smooth inversion (thin black line) and with the roughness penalty cut at the top and bottom of the reservoir (thick black line). All inversions fit the data to rms 1.0.

layer perturbations. Offshore sediment compaction often can be represented by an exponential depth function (e.g., Bahr et al., 2001). Here the porosity function $\phi(z)$ is chosen to be

$$\phi(z) = 0.05 + 0.6e^{-z/1500}, \tag{12}$$

so that porosity at the seabed is 0.65 and asymptotes at depth to 0.05. Variations in lithology and grain size are simulated by applying a random perturbation of 0% through 25% to the porosity of each layer. The conductivity σ of each layer then is assigned using Archie's law,

$$\sigma = \sigma_f \phi^2, \tag{13}$$

where σ_f is the conductivity of the pore fluid. The pore-fluid conductivity will depend on the temperature T, and here is set to obey a relation valid for seawater salinity,

$$\sigma_f = 2.903916(1 + 0.0297175T$$
$$+ 0.00015551T^2 - 0.00000067T^3) \tag{14}$$

(Constable et al., 2008).

The effect of compaction is to decrease porosity and hence conductivity at depth. However, increases in temperature and pore-fluid conductivity with depth can somewhat offset the effects of decreased porosity. The temperature is set to 1°C on the seabed and follows a linear geothermal gradient of 25°C/km, as determined for sediments offshore San Diego through joint interpretation of CSEM and deep-tow gravity data (Constable et al., 2008). Two reservoirs are embedded in this model. In addition to the canonical reservoir, a thinner and less resistive reservoir of 20-m thickness and 10-ohm-m resistivity is also considered. These two models are shown in Figure 10.

Synthetic inline B_x, E_y, and E_z data were generated at 0.1 and 1.0 Hz and inverted using the 75 inversion layers as used in the previous studies. For both models, a smooth inversion and an inversion with the roughness penalty cut along the top and bottom of the reservoir are shown in Figure 10. For the canonical reservoir, the smooth inversion recovers the reservoir nearly as well as the simpler background conductivity model considered in Figure 7. The general trend of increasing resistivity with depth is reproduced well, but the shallow section of the inversion contains significant wiggles in resistivity, although these mostly remain within the bounds of the true layer resistivities. The inversion with the cut roughness penalty recovers the reservoir resistivity as 103 ohm-m (a 3% error compared with the true resistivity) and shows good improvement in the resolution of the average sediment resistivity directly above the reservoir, but the shallowest portion of the model contains nearly the same structure as the smooth inversion.

For the smaller reservoir shown on the right side of Figure 10, the smooth inversion again follows the general trend of the background resistivity. At the depth of the reservoir is a slightly larger increase in resistivity, but this feature is highly smeared out in depth and would be difficult to interpret as a reservoir, given the presence of the shallower variability. Although not shown here,

two additional smooth inversions were performed for this model. One used more frequencies (0.1, 0.3, 1.0, 3.0, and 10.0 Hz), and the other jointly inverted all components of inline and broadside data. Both inversions produced models with the same general features as just described, hence suggesting that this additional data is of limited value.

The inversion with the roughness penalty removed on the reservoir boundaries clearly identifies the presence of this smaller reservoir, although its resistivity is too large by about a factor of two. The nature of the shallow variability in all of these inversions is intriguing, and this is likely related to the transversely isotropic conductivity created by the thin layering planes. Although not considered here, some improvement might be possible by allowing for conductivity anisotropy in each inversion model layer.

Inversion with a stratified seawater conductivity

The final model study considers the effect of seawater resistivity on the inversion models. The ocean has a stratified resistivity profile as a result of its thermal structure, whereby hotter water near the sea surface is more conductive than deeper cold water, as shown by equation 14. Other factors such as ocean currents, upwellings, and river outflows can further control seawater resistivity through thermal and salinity variations. Figure 11 shows an example of an oceanic resistivity profile measured by a Valeport conductivity meter offshore Hawaii (Myer et al., 2006). The seawater resistivity varies by about 50% over the 1-km-depth range, with most of the gradient occurring in the upper 500 m.

Although it is commonplace to measure the seawater profile during CSEM surveys using expendable conductivity-temperature-depth probes, the studies here stress the importance of including these data in numerical models because the seawater resistivity impacts CSEM responses in many ways. Because the transmissions are generated in the seawater, the fields diffusing into the seafloor will depend on the local seawater resistivity around the transmitter. In addition, long-offset CSEM responses can have a significant component of energy that has traveled through the air (e.g., Constable and Weiss, 2006). In 1D, the coupling of energy between the air, sea, and seabed can be represented as an infinite sum of terms corresponding to reflections off the seabed and sea surface (e.g., Chave and Cox, 1982; Andreis and MacGregor, 2008), so long-offset fields will be sensitive to the resistivity structure of the entire seawater column.

The seawater profile shown in Figure 11 was added to the canonical reservoir model, and synthetic 0.1- and 1.0-Hz data for inline transmissions were generated in the manner described earlier. Three inversion tests were conducted, and Figure 12 shows the results. The first test included the true seawater conductivity profile as 20 fixed layers in the inversion model. This inversion recovers the resistive reservoir layer with about the same accuracy as shown earlier for the canonical model with a uniform seawater resistivity. In the second and third tests, the inversion was allowed to solve for the seawater resistivity.

For the second test, the 1-km ocean was parameterized as a single free layer, in addition to the standard free layers below the seabed. This inversion could not find an acceptable model fit and stopped with an rms misfit of 3.6 after 100 iterations. The resulting model still contains the resistive reservoir, but there is substantially more

variation in the sediment resistivity above the reservoir, and a false increase in resistivity below the reservoir. The single seawater layer was found to be about 0.29 ohm-m.

For the third test, the ocean was divided into 20 free layers to determine if the inversion could be also used to recover the seawater resistivity profile. This inversion could fit the data to rms 1.0, but it performed significantly poorer at recovering the reservoir. The peak resistivity is slightly deeper than the reservoir, and the thickness of the resistor is substantially wider. However, as shown close-up in Figure 11, the seawater resistivity profile was recovered to about 5%–10% relative error. The largest error and variability in the seawater resistivity occurs near the depth of the transmitter (0.975 km), where it
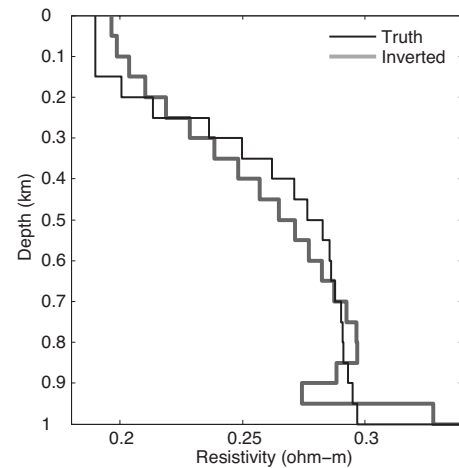

Figure 11. A seawater resistivity profile measured offshore Hawaii (black line), along with a synthetic test of inverting for seawater resistivity (gray line; close-up of the results shown in Figure 12).
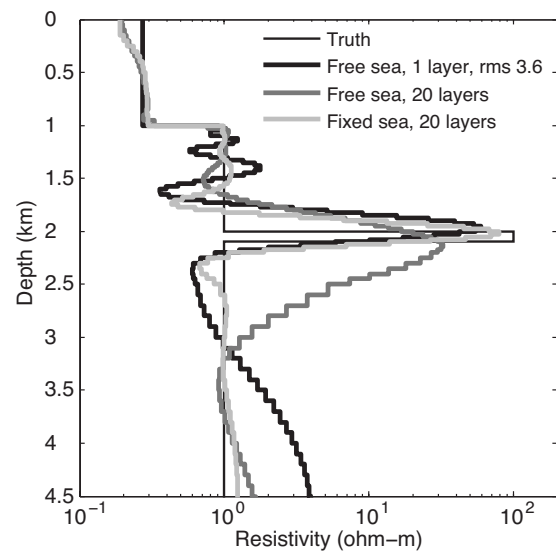

Figure 12. The effect of seawater resistivity on 1D inversion. All inversions used B_x, E_y, and E_z data for inline (y) transmissions at 0.1 and 1.0 Hz. The inversions with 20 sea layers (fixed and free) fit the data to rms 1.0, whereas the inversion with a single free sea layer could achieve only rms 3.6. A close-up of the inversion with 20 free sea layers is shown in Figure 11.

appears that the inversion is trading off penalty for structure in the seawater with the penalty associated with the less-well-imaged reservoir.

These studies demonstrate the importance of measuring the seawater resistivity profile. A stratified ocean resistivity does not impede the resolution of subsea structure so long as it is known and included as fixed structure in the inversion. However, failure to include the stratified seawater can severely degrade the accuracy of inversions. In particular, when only a single layer was used for the ocean, the inversion model was corrupted by artificial high- and low-resistivity variations above the reservoir, and these could be attributed incorrectly to sediment porosity variations, anisotropy, or the presence of conductive saline brines. The inversion can be used to solve for the seawater resistivity profile to about 5%–10% error, but there is clearly a strong trade-off between inaccuracies in the recovered seawater profile and loss of resolution of the reservoir target.

CONCLUSIONS

Synthetic inversion studies using the 1D CSEM forward and inverse modeling algorithms presented here have demonstrated the inherent resolution of various CSEM configurations to thin resistive layers representative of offshore hydrocarbon reservoirs. For the simple 1D models considered here, inversion of only two transmission frequencies spaced about a decade apart produces better resolution than inverting either frequency alone. Further increasing the frequency content does not produce an increase in resolution of the resistive layers, but it does offer a subtle increase in resolution of deeper structure. In practice, frequency studies such as this could be performed for specific structures to guide survey specifications on the frequency content of a transmitter waveform.

Systematic inversion of the three fundamental transmitter orientations shows that an inline horizontal electric dipole provides superior resolution to either broadside or vertical transmitters. This is advantageous for field surveys because an inline tow of a horizontal antenna allows for a more economical collection of data than for a broadside tow, and there are serious technical challenges associated with towing a vertical antenna through the seawater. Inversion of the horizontal electric and magnetic fields for any transmitter orientation provides better resolution than inversion of the vertical fields. Separate inversions of horizontal electric and magnetic fields perform equally well at recovering the reservoir, and there is no improvement in resolution from jointly inverting both fields, suggesting that instrumentation that records only a single field type might be adequate for certain exploration applications.

Smooth inversion for a multiple resistive layer model recovers the presence of all resistive layers, and shallow thin resistive structures do not impact the ability to detect deeper reservoirs. Although higher resistivity shallow layers must be studied, this finding is in agreement with previous forward modeling studies suggesting that deeper reservoirs might be detected beneath shallow gas hydrates. Although smooth inversion can be useful for detecting resistive layers, the accuracy of recovered resistivity values was improved substantially by including layer boundaries as a priori constraints in the inversion, demonstrating the importance of integrating structural constraints available from seismic interpretation into CSEM modeling efforts. Another factor for obtaining optimal target resolution is to include the seawater resistivity profile as fixed structure in the inversion. If the seawater is assumed incorrectly to be a homogeneous layer, spu-

rious shallow structures can be created above the reservoir and could lead to an incorrect structural interpretation.

Finally, it is worth bearing in mind that these conclusions are based on 1D models. Although these might be representative of some offshore environments, many places contain complex 2D and 3D structures and anisotropic conductivities. Three-dimensional model responses can show a significant departure from their 1D analogs, and future synthetic 2D and 3D inversion studies should consider if the conclusions reached here are valid for such increased complexity.

APPENDIX A

POTENTIAL FORMULATION FOR A HORIZONTAL ELECTRIC DIPOLE

The ordinary differential equation for the Hankel transform kernel is obtained by inserting equations 3 and 4 into equation 2, and taking the 2D Fourier transform with respect to the x- and y-directions, giving

$$-\frac{d^2\hat{\mathbf{A}}}{dz^2} + \gamma^2\hat{\mathbf{A}} = \mu\hat{\mathbf{J}}_s, \qquad (\text{A-1})$$

where $\hat{\mathbf{A}}$ is the Fourier-transformed vector potential, $\gamma^2 = \lambda^2 - i\omega\mu\sigma$, $\lambda^2 = k_x^2 + k_y^2$, and k_x and k_y are the spatial wavenumber variables of the Fourier transform. Once an analytic solution to equation A-1 has been obtained, the spatial domain solution is found by evaluating the Hankel transform expression in equation 5.

For a horizontal electric dipole pointing in the y direction, the Fourier-transformed vector potential has the form $\hat{\mathbf{A}} = (0,\hat{A}_y,\hat{A}_z) = (0,\hat{A}_y,\partial/\partial y\hat{\Lambda}_z)$, with Hankel transform expressions

$$A_y(\mathbf{r}) = \frac{1}{2\pi}\int_0^\infty \hat{A}_y(\lambda,z)J_0(\lambda r)\lambda d\lambda, \qquad (\text{A-2})$$

$$A_z(\mathbf{r}) = \frac{1}{2\pi}\frac{\partial}{\partial y}\int_0^\infty \hat{\Lambda}_z(\lambda,z)J_0(\lambda r)\lambda d\lambda. \qquad (\text{A-3})$$

Potentials $\hat{A}_y$ and $\hat{\Lambda}_z$ are cylindrically symmetric. In layer i, the potentials have the form

$$\hat{A}_{y,i} = a_i e^{\gamma_i(z-z_{i+1})} + b_i e^{-\gamma_i(z-z_i)} + \delta_{ij}\frac{\mu}{2\gamma_j}e^{-\gamma_j|z-z_s|},$$

$$(\text{A-4})$$

$$\hat{\Lambda}_{z,i} = c_i e^{\gamma_i(z-z_{i+1})} + d_i e^{-\gamma_i(z-z_i)}$$

$$- \frac{\gamma_i}{\lambda^2}(a_i e^{\gamma_i(z-z_{i+1})} - b_i e^{-\gamma_i(z-z_i)}), \qquad \text{(A-5)}$$

where z_i is the top depth of layer i and $\gamma_i^2 = \lambda^2 - i\omega\mu\sigma_i$. The dipole resides in layer j at depth z_s and is added to the potential according to the Kronecker delta δ_{ij} in equation A-4.

Note that the upward attenuation coefficients a_i and c_i are defined at the base of the layer, and the downward attenuation coefficients b_i and d_i are defined at the top of the layer; thus the potential is represented in terms of decaying exponentials. The advantage of this approach is that it avoids positive exponents, which can exceed numerical representation for excessively thick or conductive layers.

Recursive expressions can be obtained for the coefficient ratios $R_i^- = b_i/a_i$ and $S_i^- = d_i/c_i$ for layers above the transmitter, and $R_i^+ = a_i/b_i$ and $S_i^+ = c_i/d_i$ for layers below the transmitter. Expressions R_i and S_i represent transverse electric and transverse magnetic reflection coefficients (e.g., Ward and Hohmann, 1988), although their definition here is subtly different because of the offset depths of coefficients a_i, b_i, c_i, and d_i. The recursive expressions are derived by applying the continuity boundary condition of tangential **E** and **B** to equations A-4 and A-5, yielding

$$R_i^\pm = \frac{(r_i^\pm + R_{i\pm1}^\pm e^{-\gamma_{i\pm1}h_{i\pm1}})e^{-\gamma_i h_i}}{1 + r_i^\pm R_{i\pm1}^\pm e^{-\gamma_{i\pm1}h_{i\pm1}}}, \qquad \text{(A-6)}$$

where

$$r_i^\pm = \frac{\gamma_i - \gamma_{i\pm1}}{\gamma_i + \gamma_{i\pm1}}, \qquad \text{(A-7)}$$

and

$$S_i^\pm = \frac{(s_i^\pm + S_{i\pm1}^\pm e^{-\gamma_{i\pm1}h_{i\pm1}})e^{-\gamma_i h_i}}{1 + s_i^\pm S_{i\pm1}^\pm e^{-\gamma_{i\pm1}h_{i\pm1}}}, \qquad \text{(A-8)}$$

where

$$s_i^\pm = \frac{\gamma_i \sigma_{i\pm1} - \gamma_{i\pm1}\sigma_i}{\gamma_i \sigma_{i\pm1} + \gamma_{i\pm1}\sigma_i}, \qquad \text{(A-9)}$$

and $h_i = z_{i+1} - z_i$ is the thickness of layer i. The $+$ symbol is used for layers below the transmitter (i.e., $i > j$), and the $-$ symbol is used for layers above the transmitter (i.e., $i < j$).

From the boundary condition that there can be only outgoing energy in the top and bottom layers, $R_1^- = S_1^- = 0$ and $R_N^+ = S_N^+ = 0$. The recursions are computed from the outermost layers inward to layer j containing the source. By applying the boundary conditions at the top and bottom of the layer, the potential coefficients in the source layer are found to be

$$a_j = (e^{-\gamma_j|z_{j+1}-z_s|} + R_j^- e^{-\gamma_j|z_j-z_s|})\frac{R_j^+ e^{\gamma_j h_j}}{1 - R_j^- R_j^+}\frac{\mu}{2\gamma_j}, \qquad \text{(A-10)}$$

$$b_j = (R_j^+ e^{-\gamma_j|z_{j+1}-z_s|} + e^{-\gamma_j|z_j-z_s|})\frac{R_j^- e^{\gamma_j h_j}}{1 - R_j^- R_j^+}\frac{\mu}{2\gamma_j}, \qquad \text{(A-11)}$$

$$c_j = (- e^{-\gamma_j|z_{j+1}-z_s|} + S_j^- e^{-\gamma_j|z_j-z_s|})\frac{S_j^+ e^{\gamma_j h_j}}{1 - S_j^- S_j^+}\frac{\mu}{2\lambda^2}, \qquad \text{(A-12)}$$

$$d_j = (- S_j^+ e^{-\gamma_j|z_{j+1}-z_s|} + e^{-\gamma_j|z_j-z_s|})\frac{S_j^- e^{\gamma_j h_j}}{1 - S_j^- S_j^+}\frac{\mu}{2\lambda^2}. \qquad \text{(A-13)}$$

Note that the positive exponent term in these formulas cancels with the negative exponents in the recursions for R_j and S_j and thus are absent in the numerical formulation. When a receiver is located in a layer other than the source layer, the potential coefficients are found simply by using either upward or downward continuation of the potentials defined in equations A-4 and A-5, along with the appropriate substitution of R_i and S_i.

APPENDIX B

POTENTIAL FORMULATION FOR A VERTICAL ELECTRIC DIPOLE

For an electric dipole pointing in the z-direction, the vector potential has the form $\hat{\mathbf{A}} = (0,0,\hat{A}_z)$, with Hankel transform expressions

$$A_z(\mathbf{r}) = \frac{1}{2\pi}\int_0^\infty \hat{A}_z(\lambda,z)J_0(\lambda r)\lambda d\lambda, \qquad \text{(B-1)}$$

where $\hat{A}_z$ has the form

$$\hat{A}_{z,i} = c_i e^{\gamma_i(z-z_{i+1})} + d_i e^{-\gamma_i(z-z_i)} + \delta_{ij}\frac{\mu}{2\gamma_j}e^{-\gamma_j|z-z_s|}. \qquad \text{(B-2)}$$

By using the recursion for $S_i^\pm$ defined in equation A-8, the potential coefficients in the source layer are found to be

$$c_j = (e^{-\gamma_j|z_{j+1}-z_s|} + S_j^- e^{-\gamma_j|z_j-z_s|})\frac{S_j^+ e^{\gamma_j h_j}}{1 - S_j^- S_j^+}\frac{\mu}{2\gamma_j}, \qquad \text{(B-3)}$$

$$d_j = (S_j^+ e^{-\gamma_j|z_{j+1}-z_s|} + e^{-\gamma_j|z_j-z_s|})\frac{S_j^- e^{\gamma_j h_j}}{1 - S_j^- S_j^+}\frac{\mu}{2\gamma_j}. \qquad \text{(B-4)}$$

The coefficients in other layers are found by using either upward or downward continuation of the potential and noting the continuity at layer interfaces.

APPENDIX C

THE JACOBIAN MATRIX J

A numerically efficient approach to forming the Jacobian matrix **J** is to analytically differentiate the Hankel transform expressions

for **E** and **B** with respect to the conductivity of each layer (e.g., Flosadottir and Constable, 1996). This leads to differentiation of the potential coefficients a_j, b_j, c_j, d_j as defined in Appendices A and B. These coefficients have the form

$$f_j = (p + qr)\frac{stu}{1 - qs}. \qquad \text{(C-1)}$$

The full derivative expressions for the sensitivity to any model layer i have the form

$$\frac{\partial f_j}{\partial \sigma_i} = \frac{stu}{1 - qs}(p' + q'r + qr') + \frac{p + qr}{1 - qs}(s'tu + st'u$$
$$+ stu') + \frac{(p + qr)stu}{(1 - qs)^2}(q's + qs'), \qquad \text{(C-2)}$$

where the ′ symbol denotes the partial derivative with respect to σ_i, and p', r', t', u' are nonzero only when $i = j$.

The terms q' and s' correspond to $\partial R_j^+/\partial\sigma_i$ and $\partial R_j^-/\partial\sigma_i$, and similarly for the recursion coefficient S_j. These can be computed rapidly by using the chain rule. For example,

$$\frac{\partial R_j^+}{\partial \sigma_i} = \frac{\partial R_j^+}{\partial R_{j+1}^+}\frac{\partial R_{j+1}^+}{\partial R_{j+2}^+}\cdots\frac{\partial R_{i-1}^+}{\partial \sigma_i}. \qquad \text{(C-3)}$$

When a receiver is located in a layer other than the source layer, the derivatives can be found by using either upward or downward propagation from the source layer j. The resulting Hankel transform expressions for the derivatives are numerically evaluated using the digital filter method referred to earlier, and the results then are scaled to give the derivative with respect to $\log_{10}\sigma$.

REFERENCES

Abubakar, A., T. M. Habashy, V. L. Druskin, L. Knizhnerman, and D. Alumbaugh, 2008, 2.5D forward and inverse modeling for interpreting low-frequency electromagnetic measurements: Geophysics, **73**, no. 4, F165–F177.

Anderson, W. L., 1982, Fast Hankel transforms using related and lagged convolutions: ACM Transactions on Mathematical Software, **8**, 344–368.

Andreis, D., and L. MacGregor, 2008, Controlled-source electromagnetic sounding in shallow water: Principles and applications: Geophysics, **73**, no. 1, F21–F32.

Bahr, D., E. Hutton, J. Syvitski, and L. Pratson, 2001, Exponential approximations to compacted sediment porosity profiles: Computers and Geosciences, **27**, 691–700.

Chave, A., and C. Cox, 1982, Controlled electromagnetic sources for measuring electrical-conductivity beneath the oceans: 1 — Forward problem and model study: Journal of Geophysical Research, **87**, no. NB7, 5327–5338.

Christensen, N. B., and K. Dodds, 2007, 1D inversion and resolution analysis of marine CSEM data: Geophysics, **72**, no. 2, WA27–WA38.

Commer, M., and G. A. Newman, 2008, New advances in three-dimensional controlled-source electromagnetic inversion: Geophysical Journal International, **172**, 513–535.

Constable, S., K. Key, and L. Lewis, 2008, Mapping offshore sedimentary structure using electromagnetic methods and terrain effects in marine magnetotelluric data: Geophysical Journal International, doi: 10.1111/j.1365–246X.2008.03975.x.

Constable, S. C., R. L. Parker, and C. G. Constable, 1987, Occam's inversion — A practical algorithm for generating smooth models from electromagnetic sounding data: Geophysics, **52**, 289–300.

Constable, S., and L. J. Srnka, 2007, An introduction to marine controlled-source electromagnetic methods for hydrocarbon exploration: Geophysics, **72**, no. 2, WA3–WA12.

Constable, S., and C. J. Weiss, 2006, Mapping thin resistors and hydrocarbons with marine EM methods: Insights from 1D modeling: Geophysics, **71**, no. 2, G43–G51.

Edwards, N., 2005, Marine controlled-source electromagnetics: Principles, methodologies, future commercial applications: Surveys in Geophysics, **26**, 675–700.

Ellingsrud, S., T. Eidesmo, S. Johansen, M. Sinha, L. MacGregor, and S. Constable, 2002, Remote sensing of hydrocarbon layers by seabed logging (SBL): Results from a cruise offshore Angola: The Leading Edge, **21**, 972–982.

Flosadottir, A., and S. Constable, 1996, Marine controlled-source electromagnetic sounding: 1 — Modeling and experimental design: Journal of Geophysical Research, **101**, no. B3, 5507–5517.

Ghosh, D. P., 1971, The application of linear filter theory to the direct interpretation of geoelectrical resistivity sounding measurements: Geophysical Prospecting, **19**, 192–217.

Gribenko, A., and M. Zhdanov, 2007, Rigorous 3D inversion of marine CSEM data based on the integral equation method: Geophysics, **72**, no. 2, WA73–WA84.

Guptasarma, D., and B. Singh, 1997, New digital linear filters for Hankel J(0) and J(1) transforms: Geophysical Prospecting, **45**, 745–762.

Hoversten, G. M., F. Cassassuce, E. Gasperikova, G. A. Newman, J. S. Chen, Y. Rubin, Z. S. Hou, and D. Vasco, 2006, Direct reservoir parameter estimation using joint inversion of marine seismic AVA and CSEM data: Geophysics, **71**, no. 5, G239–G248.

Kong, F. N., 2007, Hankel transform filters for dipole antenna radiation in a conductive medium: Geophysical Prospecting, **55**, 83–89.

Li, Y., and K. Key, 2007, 2D marine controlled-source electromagnetic modeling: Part 1 — An adaptive finite element algorithm: Geophysics, **72**, no. 2, WA51–WA62.

Løseth, L. O., and B. Ursin, 2007, Electromagnetic fields in planarly layered anisotropic media: Geophysical Journal International, **170**, 44–80.

MacGregor, L., and M. Sinha, 2000, Use of marine controlled-source electromagnetic sounding for sub-basalt exploration: Geophysical Prospecting, **48**, 1091–1106.

Mittet, R., and T. Schaug-Pettersen, 2008, Shaping optimal transmitter waveforms for marine CSEM surveys: Geophysics, **73**, no. 3, F97–F104.

Myer, D., S. Constable, and K. Key, 2006, Electromagnetic exploration of the Loihi seamount: Eos Trans., American Geophysical Union 87(52), Fall Meeting Suppl., Abstract No. V13A-0643.

Parker, R. L., 1994, Geophysical inverse theory: Princeton University Press.

Stoyer, C. H., 1977, Electromagnetic fields of dipoles in stratified media: IEEE Transactions on Antennas and Propagation, **25**, 547–552.

Um, E. S., and D. L. Alumbaugh, 2007, On the physics of the marine controlled-source electromagnetic method: Geophysics, **72**, no. 2, WA13–WA26.

Wait, J. R., 1982, Geo-electromagnetism: Academic Press.

Ward, S. H., and G. W. Hohmann, 1988, Electromagnetic theory for geophysical applications, *in* M. N. Nabighian, ed., Electromagnetic methods in applied geophysics, SEG, 131–312.

Weidelt, P., 2007, Guided waves in marine CSEM: Geophysical Journal International, **171**, 153–176.

Weiss, C., 2007, The fallacy of the "shallow-water problem" in marine CSEM exploration: Geophysics, **72**, no. 6, A93–A97.

Weiss, C. J., and S. Constable, 2006, Mapping thin resistors in the marine environment: Part 2 — Modeling and analysis in 3D: Geophysics, **71**, no. 6, G321–G332.

Xiong, Z., 1989, Electromagnetic fields of electric dipoles embedded in a stratified anisotropic earth: Geophysics, **54**, 1643–1646.

Zhdanov, M. S., 2002, Geophysical inverse theory and regularization problems: Elsevier Science.